

The Relevance of Measurement Systems Analysis

A Procter & Gamble Case Study on
MSA Methodology and Applications

DATE

**OCTOBER
10 AND 12**

TIME

**16:00 CET,
10 am EST**



**CHRISTIAN
NEU**

Scientist
Procter & Gamble



**JERRY
FISH**

Systems Engineer
JMP



**JASON
WIGGINS**

Senior Systems
Engineer
JMP

[Register now](#)

Heterophase Grain Boundary-Rich Superparamagnetic Iron Oxides/Carbon Composite for Cationic Crystal Violet and Anionic Congo Red Dye Removal

Konthoujam Priyananda Singh, Boris Wareppam, Raghavendra Karkala Gururaj, Ningthoujam Joseph Singh, Aderbal Carlos de Oliveira, Vijayendra Kumar Garg, Subrata Ghosh,* and Loushambam Herojit Singh*

Iron oxide-based nanostructures receive significant attention as efficient adsorbents for organic dye removal applications. Herein, iron oxide/carbon composite with well-defined heterophase grain boundaries is synthesized by a simple precipitation method and followed by calcination. The local structure, spin dynamics, and magnetic properties of heterophase iron oxides/carbon composite are thoroughly investigated to explore its cationic and anionic dye removal capability. To validate the effectivity of the presence of heterogeneous grain boundaries, iron oxide/carbon nanocomposite with homogeneous grain boundaries is also examined. For an initial dye concentration of 50 mg L^{-1} , pH 7, and adsorbent dose of 0.2 g L^{-1} , the hetero-IOCC exhibits a removal capacity of 71.63 and 140.19 mg g^{-1} for the cationic crystal violet and the anionic Congo red dyes, respectively. These values are significantly greater than those exhibited by as-synthesized imidazole-capped superparamagnetic $\alpha\text{-Fe}_2\text{O}_3$, 48.15 and 53.19 mg g^{-1} ; and homophase iron oxide/carbon nanocomposite, 12.51 and 17.95 mg g^{-1} , respectively. Adsorption isotherms and kinetic studies indicate that the Langmuir isotherm model is found to be an appropriate model following the Elovich kinetic model. A detailed dye adsorption investigation on the pH effect, thermodynamic parameters, coexisting ionic effect, and reusability is also carried out.


1. Introduction

Water, the elixir of life, contributes nearly 78% of the total Earth's surface and serves as the critical component of the living world. However, the pollution of water is a grave concern in recent times. A large amount of organic dyes used in different industries like textile, paper, photography, leather, cosmetics, etc., and huge effluents in water bodies are one of the major causes of environmental and health problems.^[1,2] A trace amount of dye (less than 1 ppm) can have significant and persistent effects for long in water.^[3] Owing to their high resistance, stability, toxicity, and inability to degrade easily, these industrial waste-water pose serious threats. This includes reduction of light penetration, decrease in visibility, and increase in chemical oxygen demand thereby limiting overall aquatic ecosystem growth and causing hazardous effect on human health. These problems demand the urgent need of developing clean, efficient, environment-friendly, and

harmless techniques to remove the organic pollutants from water bodies.^[4] During the last few decades, various physiochemical

K. P. Singh, B. Wareppam, N. J. Singh, L. H. Singh
Department of Physics
National Institute of Technology Manipur
Langol 795004, India
E-mail: herojit@nitmanipur.ac.in

K. G. Raghavendra
Department of Physics
Manipal Institute of Technology
Manipal Academy of Higher Education
Manipal, Karnataka 576104, India

 The ORCID identification number(s) for the author(s) of this article can be found under <https://doi.org/10.1002/adem.202300354>.

© 2023 The Authors. Advanced Engineering Materials published by Wiley-VCH GmbH. This is an open access article under the terms of the Creative Commons Attribution License, which permits use, distribution and reproduction in any medium, provided the original work is properly cited.

DOI: 10.1002/adem.202300354

A. C. de Oliveira, V. K. Garg
Institute of Physics
University of Brasília
Brasília, DF 70919-970, Brazil

A. C. de Oliveira, V. K. Garg
Universidade Estadual de Goiás
Campus Anápolis de Ciências Exatas e Tecnológicas Henrique Santillo
CEP: 75132-400, Anápolis, GO, Brazil

S. Ghosh
Micro and Nanostructured Materials Laboratory – NanoLab
Department of Energy
Politecnico di Milano
via Ponzio 34/3, 20133 Milano, Italy
E-mail: subrata.ghosh@polimi.it

and biological techniques like advanced oxidation process, chemical precipitation, flocculation/coagulation, membrane technology, thermal treatment, biodegradation, etc. have been applied to eliminate organic pollutants from water bodies.^[5] These techniques suffer certain limitations like high cost, generation of secondary pollutants, etc. So, adsorption is regarded to be one of the most pertinent and workable alternative methods due to its easy applicability, cost-effectiveness, utmost efficiency, and environment-friendly characteristics.^[6,7]

Various attempts were made for the development of low cost, efficient, and right adsorbent for removing organic dyes from wastewater. Some of the common adsorbent materials are based on carbon, zeolite, biopolymers, metal oxides, etc.^[8] Among, iron oxide nanoparticles (IONPs) like γ -Fe₂O₃ and α -Fe₂O₃ are much popular owing to their unique features, such as great biocompatibility, low synthetic cost, simplicity of functionalization, large magnetic susceptibility, large specific surface area, chemical stability, biocompatibility, amphoteric surface function, and excellent catalytic adsorption with greater regenerative capacity.^[9,10] However, IONPs are prone to oxidation on being exposure to air.^[11] The poor stability of nanoparticles (NPs) leads to aggregation of adsorbents and often limits their application in dye removal. Another major issue with these magnetic iron oxide NPs (γ -Fe₂O₃ and Fe₃O₄) is that they are often transformed into nonmagnetic iron oxide phases like hematite (α -Fe₂O₃) under various environmental conditions over a long period of time or under the influence of high temperature.^[12] In addition, most of the industrial effluents practically include both cationic dyes (crystal violet (CV), methylene blue (MB), etc.) as well as anionic dyes (Congo red (CR), methyl orange (MO), Eriochrome black T, etc.). However, most of the adsorbents are highly selective in either of the dyes and reject the other types of dyes.^[13] For example, flower-like core-shell Fe₃O₄/MnO₂ composites, synthesized by hydrothermal process, could exhibit a removal percentage of 95% for CR, but its removal efficiencies were below 15% for CV, MO, MB, and Rhodamine B.^[14] Moreover, Fe₃O₄ NPs were functionalized by the co-precipitation method using multi-carboxylate organic ligands, which exhibit 97% removal in CR dyes but, only 14% removal for CV and 9% for MO dyes.^[15]

To tackle these challenges, surface coating of these NPs with polymers, carbon layers and organic ligands is one of the probable solutions in addition to enhancing the surface reactivity and adsorption capacity further.^[16–19] The strong bonding between the embedded NPs and graphene oxide and the possible coexistence of hematite and magnetite were proposed to be beneficial for dye removal applications.^[20] The enhanced dye adsorption by carbon compounds, however, has an inherent limitation of carbon, being nonmagnetic and not suitable for separation for reusability. This could be addressed by incorporating magnetic nanoparticles like magnetite into adsorbent material. Here, metal oxide-based nanostructures with various morphology and exciting physicochemical properties are anticipated as promising materials for the removal of the cationic and anionic dyes.^[21–23] Interestingly, the presence of both magnetic and nonmagnetic interlayers can also alter the interphase coupling and reversal mechanism, which plays a crucial role in the synchronous behavior of interphase materials.^[24,25] It is reported that the presence of carbon content in the heterophase junction can be tuned by adjusting the activation temperature of the

precursor, which uplifts the photocatalytic hydrogen evolution.^[26] Composite with heterophase grain boundary (GB) or interphase structures in nanomaterial can affect the physicochemical properties of nanomaterial owing to their high energy nature and changing electronic environment along the interphase boundaries.^[27] Basically, engineering the heterophase grain boundaries in nanocomposites may lead to the creation of lattice defects and modification of charge carriers along the boundaries. Thus, these charged states and lattice defects may provide favorable conditions for attacking positively and negatively charged dyes simultaneously and the heterophase grain boundaries serve as active site to bind the chemical groups mediating dye adsorption effectively.^[28,29]

With this background, carbon-containing iron oxide with heterophase grain boundaries is synthesized using thermal treatment on imidazole-capped superparamagnetic (SPM) α -Fe₂O₃. The local structural evolution from imidazole-capped SPM α -Fe₂O₃ to iron oxide/carbon nanocomposite with heterophase grain boundaries (hetero-IOCC) and then iron oxide/carbon nanocomposite with homophase grain boundaries (homo-IOCC) is investigated with the help of X-ray diffraction (XRD), high-resolution transmission electron microscopy (HRTEM), Fourier transform infrared spectrometer (FTIR), X-ray photoelectron spectroscopy (XPS), vibrating sample magnetometer (VSM), thermogravimetric analysis (TGA), and Mössbauer spectroscopy. The plausible mechanism of local structure evolution during the decomposition of the imidazole attached to the surface of α -Fe₂O₃ is discussed. We envisaged the stability of iron oxide/carbon composite with heterophase grain boundaries under a toxic dye environment without transforming its phase and its suitability toward potential utilization as an active material for removing both cationic and anionic dyes effectively compared to its homogeneous counterpart (homo-IOCC) or functionalized IONPs.

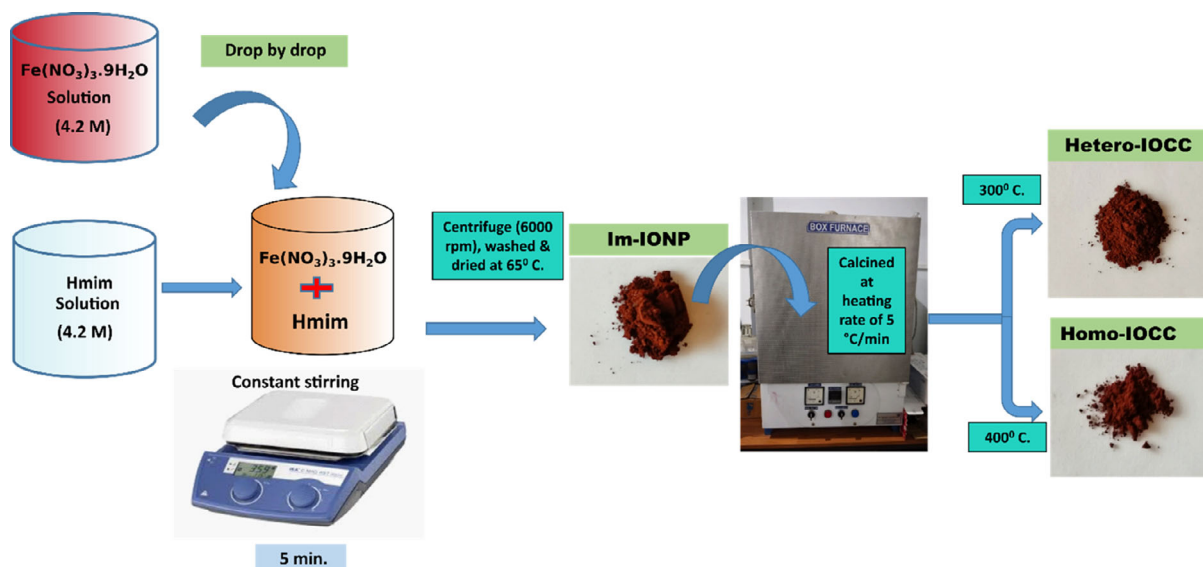
2. Experimental Section

2.1. Materials

Fe(NO₃)₃·9H₂O (98% purity), purchased from Merck Life Science Pvt. Ltd., India, and 2-methyl imidazole (Hmim) (99% purity), purchased from Sigma Aldrich, were used as the precursors. CV dye and CR dye were from HiMedia Laboratories Pvt. Ltd. HCl (min. guarantee assay 35%), NaOH (99% purity), NaCl (99% purity), and MgCl₂ (98% purity) were purchased from Rankem, SRL, HiMedia Laboratories and Merck Specialities Pvt. Ltd., respectively. All the reagents used in the experiment were employed without further purification and they were of analytical grade. Double-distilled water was used in the whole experimental process.

2.2. Nanocomposite Preparation

An aqueous solution of Fe(NO₃)₃·9H₂O (4.2 M) was mixed dropwise to the aqueous solution of Hmim of the same molarity. The two solutions were kept at magnetic stirring for 5 min until a dark reddish-colored precipitate was formed. The precipitate was subsequently separated and collected using a centrifuge (6000 rpm for 5 min). The collected precipitate was washed



Scheme 1. Schematics of preparation methodology of hetero-IOCC and homo-IOCC from Im-IONP.

several times to remove the excess unreacted imidazole. The imidazole-capped iron oxide NPs collected were dried in an oven for 6 h at around 60 °C and named as Im-IONP. The as-synthesized Im-IONP samples were subjected to thermal treatment using a conventional oven at 300 °C for 1 h duration with a heating rate of 5 °C min⁻¹. Finally, the samples were naturally cooled down at room temperature and powdered properly using a mortar pestle to get hetero-IOCC (Scheme 1). A similar procedure was carried out to obtain the homo-IOCC except the calcination temperature was 400 °C.^[30]

2.3. Material Characterization

Phase and crystallographic information of the given samples were analyzed using XRD (Bruker-D8 advance-USA) with Cu K_α radiation of wavelength 1.54056 Å and HRTEM (Tecnai G2, F30 with 300 kV accelerating voltage). The particle size distribution analysis was carried out by measuring particle size using ImageJ software. FTIR (Perkin Elmer-USA) was used to investigate the vibrational properties of the powders in attenuated total reflection mode in the range 400–4000 cm⁻¹. Mössbauer spectroscopy was utilized in transmission mode by using a ⁵⁷Co (Rh) source with an initial activity of 25 mCi (Wissel, Germany). The magnetic characteristics of as-synthesized Im-IONP, hetero-IOCC, and homo-IOCC were analyzed using VSM model (Lake Shore VSM 7410-USA) at room temperature. XPS measurement was performed for the hetero-IOCC sample on a PHI 5000 Versa Probe III- Japan equipped with Al K_α-945 monochromatic radiation source. TGA and derivative thermogravimetry (DTG) were carried out for Im-IONP sample by a TGA (NETZSCH STA 449 F3) equipped with a high-temperature furnace in the temperature range from 20 to 1000 °C at the heating rate of 10 °C min⁻¹ (in argon gas environment). The average pore diameter and surface area were determined by nitrogen adsorption and desorption methods using BELSORP-maxII (S/N 175, Version 2.0.1.1). The Brunner–Emmett–Teller

(BET) and Barrett–Joyner–Halenda (BJH) methods were employed to measure the surface area and pore size of samples. Zeta potentials were also measured by using Malvern Zetasizer Nano-ZS90.

2.4. Adsorption Experiments

The adsorption study of the CR and CV dyes was carried out by using a UV–vis spectrophotometer (Shimadzu-1800-Japan) in the wavelength range of 400–900 nm. The adsorption activities of the samples were assessed by measuring adsorption capacities and removal percentage (%) of CV and CR in an aqueous solution. For the batch adsorption experiment, 0.2 g L⁻¹ of Im-IONP, hetero-IOCC, and homo-IOCC samples were added to an initial dye concentration of 10 mg L⁻¹ at the neutral pH condition. The samples were kept in a dark room without stirring and measurements were carried out to ensure that the equilibrium was achieved in the dark room. The concentration of the dyes was calculated from the maximum absorbance peak corresponding to λ = 498 nm for CR and λ = 583 nm for CV. The experiment was done at different intervals of time for about 14 h to attain the equilibrium. It was observed that a decrease in absorbance was obtained within the time frame.

The adsorption capacity was calculated based on the equation below:

$$q_t = \frac{(C_0 - C_t)}{m} V \quad (1)$$

where C₀ and C_t represent the initial concentration and the concentration at a certain time interval of CV and CR, respectively (mg L⁻¹), V is the volume of the solution (mL), and m is the mass of the sample (mg). For equilibrium, C_t = C_e; q_t = q_e, where C_e and q_e are equilibrium concentration and equilibrium adsorption capacity.

The removal efficiency of various samples was calculated by using the relation

$$\text{Removal Percentage (\%)} = \frac{C_0 - C_t}{C_0} \times 100 \quad (2)$$

2.5. Reusability of Adsorbent

The reusability of adsorbent is one of the important parameters of the adsorption process from an economic and environmental point of view. The dye loaded on adsorbent was washed with ethanol three times with constant shaking and the adsorbent was dried using the oven at 70 °C for 1 h. Thus, the used adsorbents could be further used for the adsorption of CR and CV in the same procedure for three repeated cycles.

3. Results and Discussion

3.1. Structural Analysis

The powder XRD pattern of hetero-IOCC is shown in **Figure 1b**. The observed characteristic diffraction peaks for hetero-IOCC at a 2θ angle of 24.2°, 33.2°, 35.6°, 40.8°, and 49.4° are assigned to the scattering from (012), (104), (110), (113), and (024) planes of α -Fe₂O₃, respectively, [JCPDS NO. 86-2368 (α -Fe₂O₃)].^[31] Whereas, the respective diffraction peaks at an angle of 30.2°, 35.5°, 43.2°, and 62.9° correspond to the scattering from (220), (311), (400), and (440) planes of γ -Fe₂O₃ [JCPDS NO. 39-1346 (γ -Fe₂O₃)].^[32] In contrast, homo-IOCC exhibits diffraction peaks

at a 2θ angle of 24.2°, 33.2°, 35.6°, 40.8°, 49.4°, 62.4°, and 64.0° assigned to the (012), (104), (110), (113), (024), (214), and (300) planes of α -Fe₂O₃ and there is no observed peaks corresponding to γ -Fe₂O₃, as shown in **Figure 1a**.^[33] The emergence of sharp peaks of higher intensities confirms the crystalline character of both hetero-IOCC and homo-IOCC. The peaks corresponding to α -Fe₂O₃ components are sharp indicating a larger crystallite size than the γ -Fe₂O₃ having comparatively broader peaks. Further, the α -Fe₂O₃ is likely to exhibit bulk-like magnetic properties, whereas γ -Fe₂O₃ is proposed to behave as a superparamagnet.^[34] Hence, it is expected to have superparamagnet features for hetero-IOCC, whereas the bulk-like magnetic features for the homo-IOCC. This statement is further strengthened by the below VSM and Mössbauer studies. As shown in **Figure 1c**, the Im-IONP exhibits a scattered spectrum with no detectable diffraction peaks, indicating a lack of crystalline nature or a very fine SPM particle size.^[35]

Figure 2a shows the HRTEM micrographs of hetero-IOCC, which confirms the heterophase GB of α -Fe₂O₃ and γ -Fe₂O₃ (represented by green and yellow lines). The radial profile analysis from the selected area electron diffraction (SAED) pattern of hetero-IOCC (**Figure 2b**) shows that the rings correspond to α -Fe₂O₃ and γ -Fe₂O₃ phases. The corresponding (hkl) values (012), (104), (113), (024), (300) of α -Fe₂O₃ (represented by yellow color) and (422), (311) of γ -Fe₂O₃ (represented by green color) marked the presence of these two phases. Moreover, inverse fast Fourier transform (IFFT) images corresponding to α -Fe₂O₃ and γ -Fe₂O₃ for the hetero-IOCC sample are obtained through image processing and displayed in **Figure 2c**. The heterophase grain boundaries of α -Fe₂O₃ and γ -Fe₂O₃ become less prominent in homo-IOCC (**Figure 2d**) as only the planes of α -Fe₂O₃ like (024), (300), (312), and (048) (represented by yellow ring) are present. In addition, the SAED pattern analysis of this sample shows the presence of the planes (000), (111), (5-3-1), and (6-20) (represented by green color) corresponding to γ -Fe₂O₃, as shown in **Figure 2e**. However, the IFFT analysis of this sample (**Figure 2f**) shows a clear indication of the absence of the γ -Fe₂O₃ phase in the homo-IOCC sample.

The HRTEM micrographs of the Im-IONP indicate that the diffused lattice fringes from the fine nanocrystals can be observed at various locations (yellow circles in **Figure 2g**). Further, the SAED pattern, as shown in **Figure 2h**, also shows diffused rings which confirms the nanocrystallinity of α -Fe₂O₃ in Im-IONP. This is in agreement with the XRD result showing scattered background and also resolves the limitation of the XRD result where crystalline phases were not confirmed. The diffraction planes of this nanocrystallinity of α -Fe₂O₃ are identified to be (110), (202), and (300). IFFT image of the (113) oriented α -Fe₂O₃ crystals is shown in **Figure 2i** along with the d -spacing of 0.221 nm corresponding to it.

The particle size distributions of the samples were also carried out through image analysis of TEM micrographs of these samples and the results are shown in **Figure 2j-l**. As expected, the size of Im-IONP was ranging from 3 to 7 nm. Due to heat treatment, the resulting iron oxide NPs exhibit much greater particle sizes, and the particles as clearly seen from **Figure 2j-l** indicate that the increment of particle size of samples follows the trend: homo-IOCC (10–70 nm) > hetero-IOCC (5–16 nm) > Im-IONP

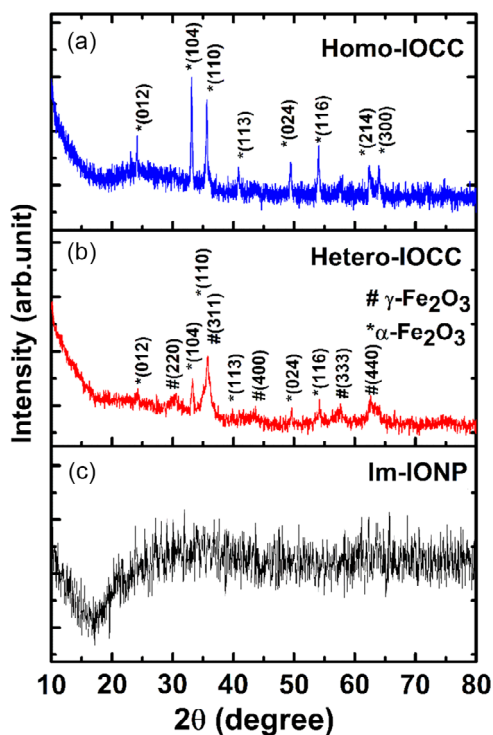


Figure 1. XRD patterns of a) homo-IOCC, b) hetero-IOCC, and c) Im-IONP.

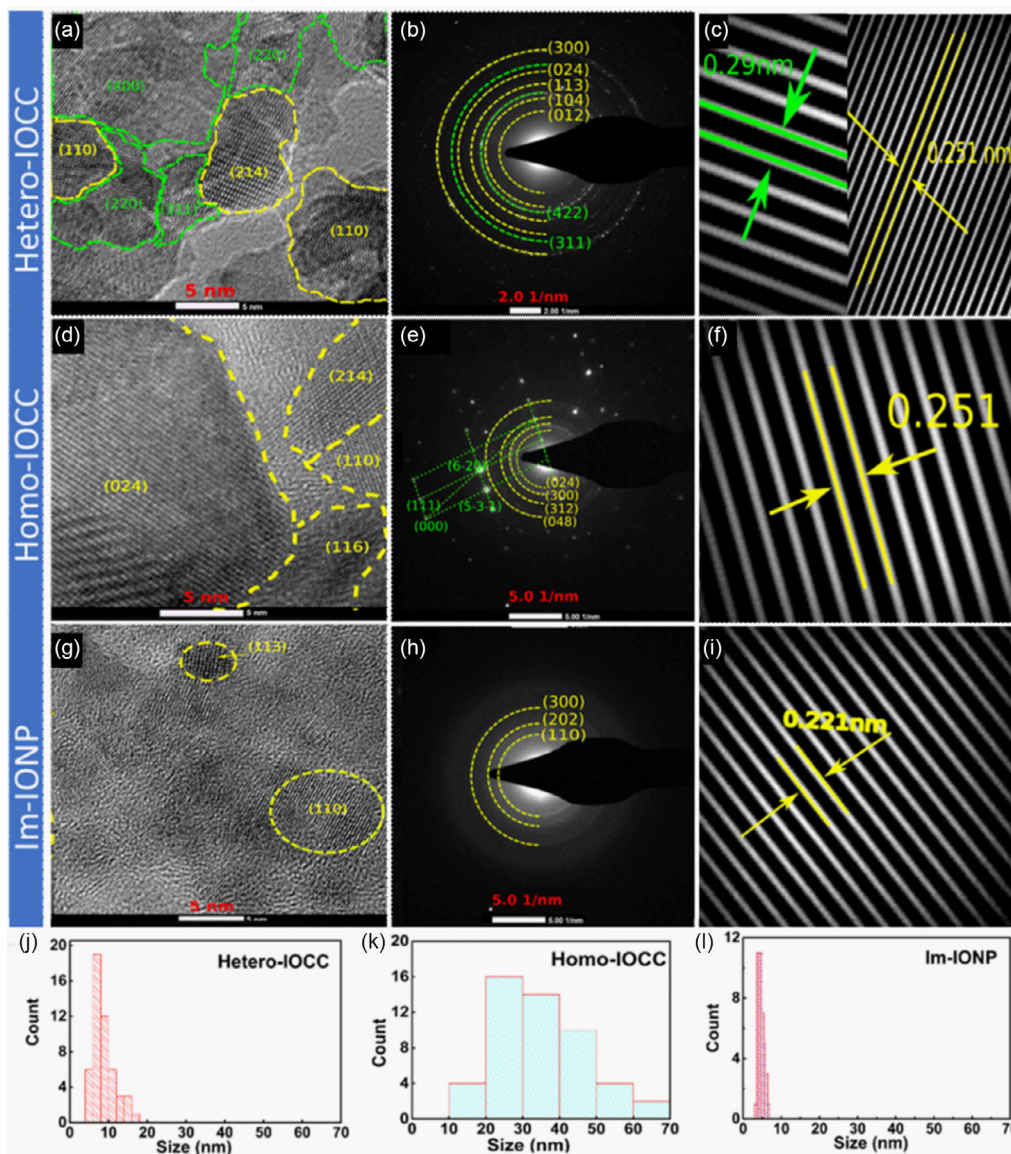


Figure 2. a) HRTEM micrographs, b) SAED patterns, and c) IFFT of (110) plane of α -Fe₂O₃ and (220) plane of γ -Fe₂O₃ for hetero-IOCC; d) HRTEM micrographs, e) SAED patterns, and f) IFFT of (110) plane of α -Fe₂O₃ for homo-IOCC; g) HRTEM micrographs, h) SAED patterns, and i) IFFT of (113) plane of α -Fe₂O₃ for Im-IONP; The particle size distribution for j) hetero-IOCC, k) homo-IOCC, and l) Im-IONP.

(3–7 nm), which can be attributed to the effect of calcination at different temperature.

The observation of very fine particles is understood due to the instant capping of the precipitated α -Fe₂O₃ by 2-methyl imidazole thereby preventing them from agglomeration. The 2-methyl imidazole under thermal treatment releases reductive gases and reduces the α -Fe₂O₃ to cubic γ -Fe₂O₃.^[36,37] Thus, with the decomposition of imidazole from the surface of iron oxide NPs at 300 °C, the nanocrystalline imidazole linked α -Fe₂O₃ NPs get partially reduced into γ -Fe₂O₃ NPs. This results to the development of a well-defined GB of γ -Fe₂O₃ NPs and α -Fe₂O₃ NPs. This process results in a mixed γ -Fe₂O₃/ α -Fe₂O₃ phases with well-defined hetero-phased GB (hetero-IOCC). The heterophase grain boundaries of γ -Fe₂O₃/ α -Fe₂O₃ become

less prominent in Homo-IOCC, which reveals that the hetero-phase structure gets transformed mostly into single phase nanostructure of α -Fe₂O₃. Further quantification of this γ -Fe₂O₃ phase will be done using Mössbauer spectroscopy in the subsequent section of this article.

3.2. Chemical Studies by XPS

As the calcination was conducted at 300 and 400 °C, the presence of carbon on the surface of iron oxide is expected. Therefore, to understand the chemical composition and bonding states of different elements present in the material after decomposition, XPS was carried out on hetero-IOCC (**Figure 3**). The characteristic peaks of C, O, N, and Fe at their corresponding binding energy

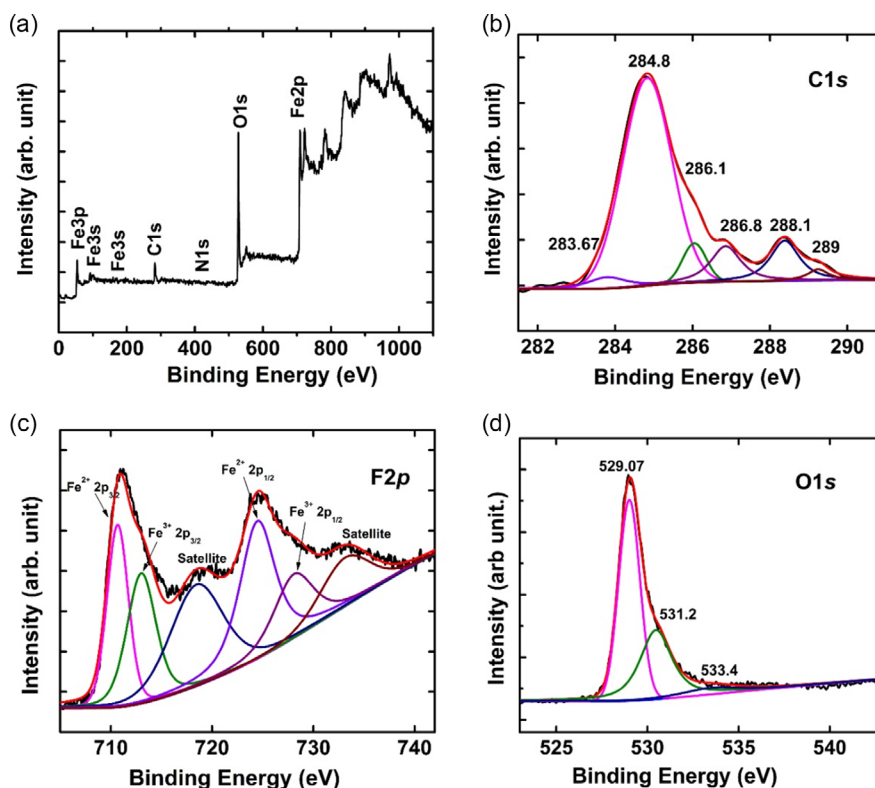


Figure 3. a) Full spectra, b) C 1s spectra, c) Fe 2p spectra, and d) O 1s spectra of hetero-IOCC.

values are seen. The C1s spectrum comprises the six peak positions with binding energies at around 283.7, 284.8, 286.1, 286.8, 288.1, and 289.1 eV corresponding to Fe–C, C–C, C–N, C–O, C=O, and O–C=O, respectively. The dominant peak at 284.8 eV (C–C) indicates that C remained present in the hetero-IOCC sample in the residue, obtained after calcination of the homo-IOCC sample at 300 °C. This indirectly suggests the breakdown of imidazole attached to the iron oxide nanoparticles, leaving carbon residues.^[38,39] Also, high-resolution spectrum of Fe2p spectra indicates two spin-orbit coupling signatures. The corresponding peaks at 710.8 and 713.3 eV represent the Fe²⁺ 2p_{3/2} and Fe³⁺ 2p_{3/2} orbits, whereas the characteristic peaks 724.3 and 726.2 eV arise due to the Fe²⁺ 2p_{1/2} and Fe³⁺ 2p_{1/2} orbits, respectively. These data are in agreement with the XRD and TEM results which predicted the structural transformation of α -Fe₂O₃ into γ -Fe₂O₃ in hetero-IOCC. Along with these four major peaks, there are two shake-up satellite peaks observed at 719.6 and 732.2 eV. Here, the greater area of 2p_{3/2} as compared to 2p_{1/2} may be due to higher spin-orbit *j-j* coupling having degeneracy 4 of Fe 2p_{3/2} as compared to degeneracy 2 of Fe 2p_{1/2}. In the O1s spectra, the main characteristic peaks at 529.07 eV can be attributed to the Fe–O bond. The binding energy peaks at 531.2 eV arise out of the oxygen defects in the iron oxide complex of the hetero-IOCC sample.^[40] The broadened peaks at 533.4 eV can be assigned to C–O bond. This peak further reaffirms the presence of carbon in the sample.^[41] The weak peaks of N 1s around 395–402 eV prove the presence of nitrogen in low quantity. However, XPS spectra of N 1s are not so significant as compared to other spectra of C1s, O1s, and

Fe2p; yet, the presence of nitrogen bond at a binding energy range of around 395–402 eV can be detected [Figure S2, Supporting Information].^[42]

3.3. Magnetic Properties

The Mössbauer spectra of Im-IONP consist of an SPM doublet experiencing Δ (Quadrupole splitting) and δ (isomer shift) of 0.73 and 0.25 mm s⁻¹, respectively (Table 1). In the Mössbauer studies, the doublet in Im-IONP transforms to two sextets and a doublet in hetero-IOCC (Figure 4a). The evolution of sextet with different B_{hf} (Mean Hyperfine field) and the doublet in hetero-IOCC is due to the varying distribution of particle size (5–16 nm) as a consequence of agglomeration during heat treatment and partial oxidation of γ -Fe₂O₃ to α -Fe₂O₃, which is also in agreement with TEM analysis. The SPM doublet of 13% is attributed to the isolated NPs with a size of less than 10 nm. The sextet with the hyperfine field of 29 T consists of 74% of the total area. This fact is attributed to the particles exhibiting high interparticle magnetic interaction and those particles having dimensions larger than the SPM regime but still experiencing large surface energy. This is plausible only when the Hmim surfactants, which prevent the particles from agglomeration, got decomposed resulting in a decrease in the interparticle distances and enhancing the magnetic interaction.^[43] The sextet with 13% of the total area experienced at 51 T, quadrupole splitting of 0.22 mm s⁻¹, and isomer shift of 0.26 mm s⁻¹ correspond to ideal bulk α -Fe₂O₃.^[44] From the variation of the

Table 1. Room temperature Mössbauer data of hetero-IOCC, homo-IOCC, and Im-IONP. Data in brackets represent the standard deviation in decimal point.

Sample	Area [%]	Isomer shift δ [mm s ⁻¹]	Mean hyperfine field, B_{hf} [T]	Quadrupole splitting, Δ [mm s ⁻¹]	Saturation magnetization, M_s [emu g ⁻¹]	Coercivity, H_c [Oe]
Hetero-IOCC	13	0.21 (0)		0.79 (1)	30.59	52.80
	13	0.26 (0)	51.0 (1)	0.22 (0)		
	74	0.23 (2)	29.0 (3)	0.01 (3)		
Homo-IOCC	100	0.26 (0)	51.3 (2)	0.23 (0)	1.18	557.40
Im-IONP	100	0.25 (0)		0.73 (0)	1.15	50.99

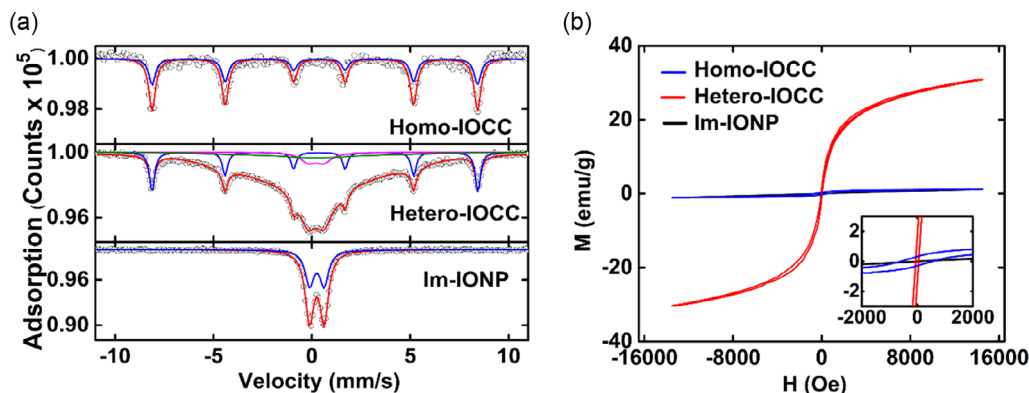


Figure 4. a) Mössbauer spectra and b) magnetic hysteresis curve for hetero-IOCC along with Im-IONP and homo-IOCC.

hyperfine field, it is understood that the particles' agglomeration occurs during the decomposition of imidazole. In the course of oxidation to α -Fe₂O₃ from γ -Fe₂O₃, the rate of agglomeration or fusion of the oxidized particle is much higher than the nucleation of γ -Fe₂O₃, which is left unoxidized. The oxidized portion of the particles, i.e., α -Fe₂O₃ from γ -Fe₂O₃ was often observed to have larger particle size as compared to the remaining metal oxides, as evident from the TEM analysis. The agglomeration effect in oxidized α -Fe₂O₃ is further observed in the homo-IOCC, which was obtained by oxidizing γ -Fe₂O₃ at 400 °C. The Mössbauer spectrum consists of a single sextet exhibiting the properties of bulk α -Fe₂O₃ with no trace of SPM particles or γ -Fe₂O₃.

The hysteresis loop (magnetization “M” vs magnetizing field “H” curve) of hetero-IOCC confirms the behavior of SPM ferromagnet (Figure 4b). The increase in magnetization may be due to the presence of the ferrimagnetic γ -Fe₂O₃ phase. At a lower magnetizing field, it exhibits a ferromagnetic straight line with an abrupt increase in magnetization. At a higher magnetizing field (14 400 Oe), it exhibits unsaturated linear magnetization, which is most probably due to the contribution of antiferromagnetic α -Fe₂O₃.^[45] Hetero-IOCC experiences the magnetization of 30.59 emu g⁻¹ at the magnetizing field of 14 400 Oe. The magnetic transition from antiferro to ferromagnet is due to the structural transformation of α -Fe₂O₃ to ferrimagnetic γ -Fe₂O₃. The MH loop of Im-IONP, in Figure 4b, shows a linear and zero coercivity. From the Mössbauer spectrum as well MH loop, the Im-IONP is confirmed as antiferromagnetic α -Fe₂O₃ experiencing SPM. The MH loop of homo-IOCC shows a similar feature to Im-IONP. This indicates the antiferromagnetism of the particles, i.e., α -Fe₂O₃. The coercivity (H_c) of the

homo-IOCC is higher than the hetero-IOCC and Im-IONP, as indicated in Table 1 (inset of Figure 4b). Thus, the Mössbauer spectrum of homo-IOCC consists of a single sextet corresponding to α -Fe₂O₃, as the presence of γ -Fe₂O₃ is below the detectable range from Mössbauer spectroscopy. It is observed that the magnetization of homo-IOCC drops significantly compared to hetero-IOCC, which may be due to the oxidation of ferrimagnetic γ -Fe₂O₃ back to nonmagnetic α -Fe₂O₃. This agrees with the Mössbauer data, as shown in Table 1.

3.4. Hetero-IOCC Formation Mechanism

To explore the formation mechanism of hetero-IOCC and homo-IOCC from Im-IONP, detailed FTIR studies were conducted. The Im-IONP precipitate was obtained as a consequence of the addition of 2-methyl imidazole (Hmim), which acts as a base, on the surface of NPs.^[46] Figure 5a shows the FTIR spectra of Hmim, Im-IONP, hetero-IOCC, and homo-IOCC samples. The peaks at 580 cm⁻¹ with a shoulder at around 626 cm⁻¹ correspond to the stretching vibration of the Fe–O bond for Im-IONP. A comparative study of FTIR spectrums of Im-IONP and Hmim shows similar vibration at 744, 826, 1110, and 1326 cm⁻¹ which correspond to the N–H wagging, out-of-plane bending, C–N stretching vibrations and in-plane bending of imidazole ring, respectively.^[47] This is understood as Hmim is attached to the surface of IONPs. However, a significant reduction in the peak intensity and a shift of imidazole peaks at 1440 cm⁻¹, which correspond to C–H rocking toward the lower wavenumber in the Im-IONP sample, were observed.

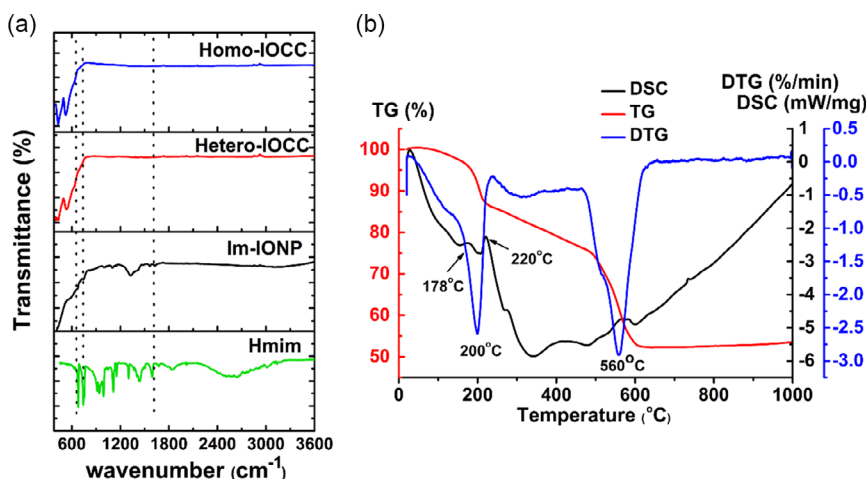


Figure 5. a) FTIR of Hmim, Im-IONP, hetero-IOCC, and homo-IOCC b) TGA, DTG, and DSC of Im-IONP.

This weakening of the bond may be due to the interaction of metal ions with Hmim during the synthesis process.^[48] Thus, the FTIR spectrums of hetero-IOCC and homo-IOCC show the absence of hydroxyl group ($-OH$) ($\approx 3440\text{ cm}^{-1}$), C–H (methyl) ($\approx 2930\text{ cm}^{-1}$), and C–H (IM) ($\approx 3137\text{ cm}^{-1}$) vibrations. These may be attributed to the breakdown of the imidazole ring, which can be further clarified by the TGA and DTG analysis. Two bands at 527 and 436 cm^{-1} (Figure 5a) were emerged in hetero-IOCC, which can be attributed to the Fe–O vibration of $\gamma\text{-Fe}_2\text{O}_3$ and $\alpha\text{-Fe}_2\text{O}_3$.^[49,50]

To complement the decomposition of 2-methyl imidazole (Hmim) and reduction of $\alpha\text{-Fe}_2\text{O}_3$, the imidazole attached SPM $\alpha\text{-Fe}_2\text{O}_3$ (Im-IONP) was investigated using TGA-DSC in Argon gas. Figure 5b shows the TG, DTG, and DSC profiles of Im-IONP in the temperature range of $20\text{--}1000\text{ }^\circ\text{C}$. TG curve clearly indicates an initial small weight loss of 4% at the temperature below $175\text{ }^\circ\text{C}$ due to the desorption of water molecules that might be present on the surface of IONP. Higher weight loss of around 11% is observed in the temperature range of around $175\text{--}218\text{ }^\circ\text{C}$. As FTIR analysis clearly shows the absence of adsorption bands around 3400 cm^{-1} corresponding to $-OH$ vibration of water molecules, the weight loss at this temperature range of around $200\text{ }^\circ\text{C}$ might be due to thermal degradation of 2-methyl imidazole ligands that surround the IONPs. This thermal degradation of the organic ligands lasts for a wide temperature range from 218 to $490\text{ }^\circ\text{C}$, resulting in a weight loss of 12%. It is expected that the decomposition of surfactants is often accompanied by the release of reducing gases such as CO and H_2 .^[51] During the calcination, these gases are believed to play a role in reducing the SPM $\alpha\text{-Fe}_2\text{O}_3$ NPs, the emergence of $\gamma\text{-Fe}_2\text{O}_3$ phase, and even to the metallic Fe.^[52] Further weight loss of 23% is observed in the temperature range of $490\text{--}600\text{ }^\circ\text{C}$.

Another important thermal property is the temperature corresponding to the maximum rate of weight loss (T_{\min}), which is defined as the peak value of the first derivative of the TG curve. The presence of a significant exothermic peak in the DTG profile around $200\text{ }^\circ\text{C}$ suggests that the degradation of the imidazole takes place in this temperature range, which is in agreement with weight loss in TG results reported by Ullah et al. DSC profile also suggests that there are two exothermic peaks at 178 and $220\text{ }^\circ\text{C}$

which could be due to the breakdown of the loosely bound outer imidazole and second the strongly bound inner imidazole, respectively.^[53] Thus, the first stage of decomposition around $200\text{ }^\circ\text{C}$ may be from the elements at the tails of the ligands attached to IONP, and the second stage of decomposition at $560\text{ }^\circ\text{C}$ is due to the releasing of the carbon deposited on the surface of iron oxide. This analysis further indicates that carbon is still present in the hetero-IOCC and homo-IOCC as both the samples were calcined at a temperature well below the range corresponding to the release of carbon. The presence of carbon is also ensured by the XPS result.

3.5. Textural Properties Using BET Analysis

The surface area of adsorbent material and the presence of active sites are critical factors for dye adsorption applications. So, the N_2 adsorption-desorption isotherm curves of the Im-IONP, hetero-IOCC, and homo-IOCC samples using BET-BJH method were shown in Figure S3, Supporting Information. The BET surface area, total pore volume, and average pore diameter of these samples are also presented in Table S1, Supporting Information. It is found that Im-IONP exhibits Type I curve while hetero-IOCC and homo-IOCC exhibit Type II curves, as per IUPAC classification. All the samples were comprised of majority of mesopores with an average pore diameter of range $2\text{--}40\text{ nm}$. It was observed that the BET surface area of Im-IONP decreased from 163.68 to $55.19\text{ m}^2\text{ g}^{-1}$ in hetero-IOCC sample and $12.78\text{ m}^2\text{ g}^{-1}$ in homo-IOCC sample. This decrease in surface area with the increase of calcining temperature could be due to the agglomeration after the breakdown of imidazole ligands attached to the iron oxide nanoparticles initially present in the Im-IONP.

3.6. Dye Removal Capacity

3.6.1. Effect of CR and CV Dye Removal Capacity

The dye removal percentage and adsorption capacity of the hetero-IOCC in comparison with homo-IOCC and Im-IONPs are shown in Figure 6a–c. The discoloration of the dye indicates

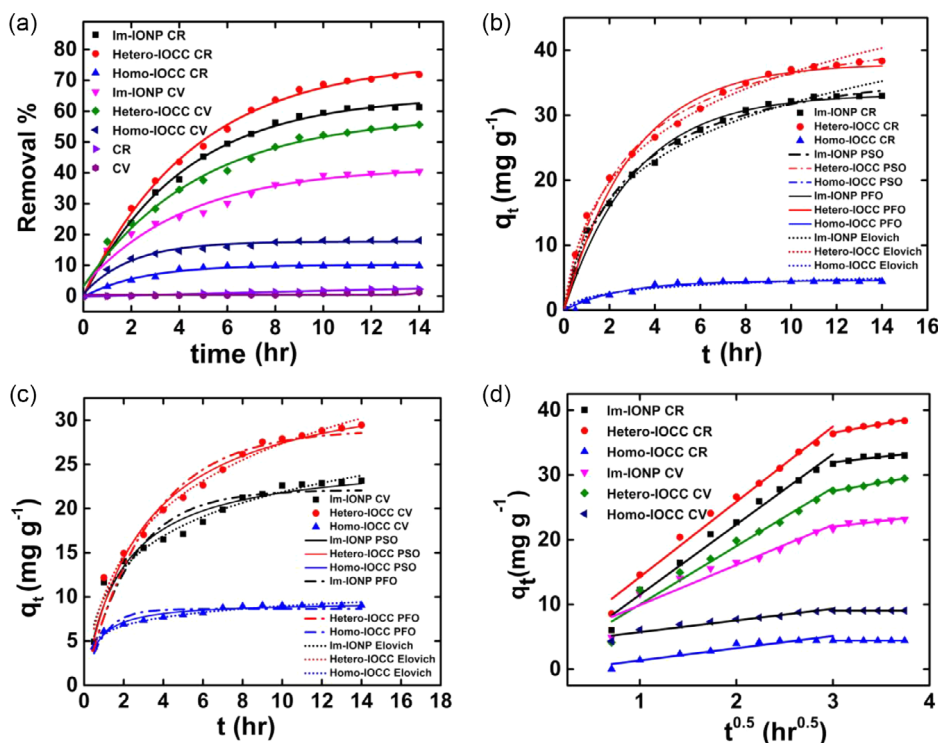


Figure 6. a) Removal percentage of CR and CV dyes for hetero-IOCC compared with Im-IONP and homo-IOCC; pseudo-first-order kinetic plot, pseudo-second-order kinetic plot, and Elovich models for the adsorption of b) CR, c) CV, and d) Weber–Morris plot. [Adsorbent dose: 0.2 g L^{-1} , initial dye concentration: 10 mg L^{-1} , pH 7].

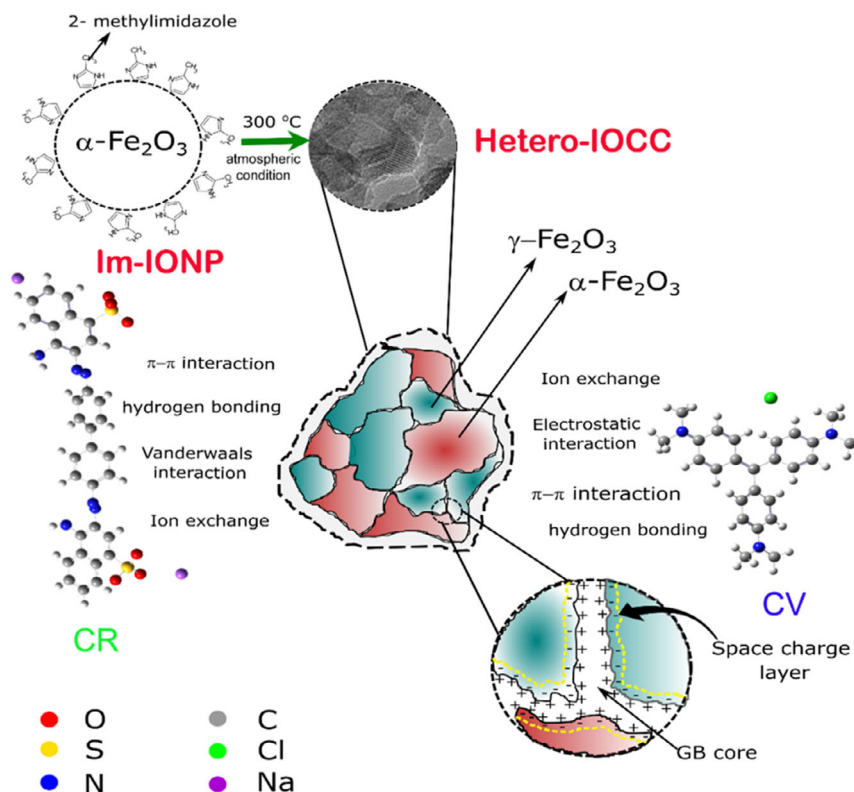
that the hetero-IOCC, homo-IOCC, and Im-IONP samples were effective for wastewater treatment. At the same experimental condition [adsorbent dose: $0.2 \times \text{g L}^{-1}$, initial dye concentration: 10 mg L^{-1} , pH 7], the CR dye adsorption capacity for hetero-IOCC was found to be higher (45.84 mg g^{-1}) than that of homo-IOCC (5.43 mg g^{-1}) and Im-IONP (40.44 mg g^{-1}). Impressively, the CV dye adsorption capacity of hetero-IOCC was also higher (35.45 mg g^{-1}) compared to that for homo-IOCC (9.41 mg g^{-1}) and Im-IONP (25.11 mg g^{-1}). The obtained adsorption result certainly elucidated the importance of the presence of heterophase grain boundaries over the homophase counterpart and the presence of both $\alpha\text{-Fe}_2\text{O}_3$ and $\gamma\text{-Fe}_2\text{O}_3$ phase over the single phase in the carbon-containing iron oxide nanocomposite. The creation of well-defined heterophase grain boundaries may lead to the creation of more defects mainly positively charged oxygen vacancies, which is in agreement with the XPS result as well. Thus, when heterophase structures are developed, positive charge potential along the grains might be enhanced, thereby inducing a negatively charged space layer owing to the space charge effect, as shown in **Scheme 2**. So, the positively charged potential along the GB core creates the active sites for adsorbing anionic dyes while the neighboring negatively charged space layer could be the reason for attaching cationic dyes.^[54] While bulk properties are dominant at the microlevel, the effect of the charged state along grain boundaries is more pronounced at the nanolevel. It has been reported that the GB effect plays a dominant role in dye adsorption.^[55] The comparatively low removal capacity of the Im-IONP sample is

because $\alpha\text{-Fe}_2\text{O}_3$ consists of a single grain capped with organic imidazole ligands, thereby reducing the interaction of the dye with iron oxide NPs. Hetero-IOCC samples, in contrast, exhibit well-defined grain boundaries with multiple phases of $\alpha\text{-Fe}_2\text{O}_3$ and $\gamma\text{-Fe}_2\text{O}_3$. The grain boundaries consist of huge defects and the boundaries of different crystallite phases may consist of higher defects compared to the single-phase boundaries. The defects at the boundaries also act as the active sites to adsorb the dye. The surface of hetero-IOCC has higher exposure and has superior removal capacity than that of Im-IONP. In contrast, Im-IONP and hetero-IOCC samples have a larger surface-to-volume ratio compared to homo-IOCC, which is evident from the TEM result of particle size comparison between these samples. Moreover, hetero-IOCC has another advantage of greater saturation magnetization than Im-IONP and homo-IOCC samples that it is sensitive to the external magnetic field and can be separated with ease to use for another cycle.

3.6.2. Adsorption Kinetic Study

To better understand the adsorption kinetics, the order of the adsorption process was determined by fitting the experimental data into the nonlinear pseudo-first-order (Equation (3)), nonlinear pseudo-second-order equations (Equation (4)) and Elovich models (Equation (5)).^[56]

$$q_t = q_e(1 - e^{-k_1 t}) \quad (3)$$



Scheme 2. Schematics of proposed dye adsorption mechanism of hetero-IOCC.

$$q_t = \frac{k_2 q_e^2 t}{1 + k_2 q_e t} \quad (4)$$

$$q_t = \frac{1}{\beta} \ln(\alpha \beta t) \quad (5)$$

where q_t and q_e are adsorption capacity at time t and steady state, respectively. k_1 and k_2 are first-order and second-order kinetic rate constants, respectively. Here, α reflects the initial absorbance and β is the dye desorption rate.

To study the diffusion model, the Weber–Morris model equation is used, which is given below:^[57]

$$q_t = k_3 t^{1/2} + I \quad (6)$$

where k_3 is the rate constant of the intraparticle diffusion model, and I is a constant for any experiment (mg g^{-1}).

To analyze the adsorption kinetics using pseudo-first-order, pseudo-second-order, and Elovich kinetic models, the nonlinear plots of q_t versus time are shown in Figure 6b,c. The coefficients of determination (R^2), derived from the fitting models have been provided in **Table 2** to show differences in goodness of fitting. In this kinetic study, the Elovich kinetic model with a higher R^2 value is found to be the better model for depicting CV and CR dye adsorption on hetero-IOCC, homo-IOCC, and Im-IONP (shown in **Table 2** and 3). This indicates that chemisorption due to electrostatic interaction between the adsorbent surface and dye particles could be the dominant factor leading to the adsorption of dyes.^[58] The value of α from the Elovich

Table 2. Parameters of pseudo-first-order, pseudo-second-order, and Elovich kinetic models for the adsorption of CV and CR dyes onto hetero-IOCC, homo-IOCC, and Im-IONP.

Sample	Pseudo-first-order			Pseudo-second-order			Elovich model		
	q_e [mg g^{-1}]	K_1 [hr^{-1}]	R^2	q_e [mg g^{-1}]	K_2 [$\text{g mg}^{-1} \text{hr}^{-1}$]	R^2	α [$\text{mg g}^{-1} \text{hr}^{-1}$]	β [g mg^{-1}]	R^2
Hetero-IOCC CV	28.94	0.31	0.90	35.45	0.01	0.98	88.86	0.11	0.98
Homo-IOCC CV	8.64	0.99	0.81	9.41	0.16	0.96	88.09	0.18	0.96
Im-IONP CV	22.11	0.42	0.89	25.11	0.02	0.96	26.86	0.17	0.97
Hetero-IOCC CR	37.94	0.33	0.90	45.84	0.0083	0.93	25.47	0.08	0.97
Homo-IOCC CR	4.56	0.40	0.94	5.43	0.085	0.95	4.46	0.09	0.98
Im-IONP CR	33.21	0.32	0.94	40.44	0.0089	0.95	21.26	0.80	0.95

Table 3. Parameters of Weber–Morris model for the adsorption of CV and CR dyes onto hetero-IOCC, homo-IOCC, and Im-IONP.

Sample name	Step-I		Step-II	
	K_3 [mg (g hr ^{0.5}) ⁻¹]	I [mg g ⁻¹]	K_3 [mg (g hr ^{0.5}) ⁻¹]	I [mg g ⁻¹]
Hetero-IOCC CV	9.01	1.00	19.65	0.37
Homo-IOCC CV	1.81	3.91	4.42	0.01
Im-IONP CV	6.20	3.68	16.78	1.74
Hetero-IOCC CR	11.62	2.62	28.50	2.67
Homo-IOCC CR	1.89	0.54	9.05	0.01
Im-IONP CR	10.85	0.64	26.82	1.71

model for the hetero-IOCC sample was found to be greater than that of homo-IOCC and Im-IONP in the case of both CV and CR dye adsorption. This indicates that hetero-IOCC has better dye adsorption performance than the other two counterparts.^[59]

In the kinetic study of dye removal, the pseudo-first-order, pseudo-second-order, and Elovich kinetic models helped in identifying the adsorption process, however, they could not identify the mass transfer and diffusion mechanism. So, the Weber–Morris model of intraparticle diffusion model was adopted, as given in Equation (6). Weber–Morris adsorption model of CV and CR (q_t vs $t^{0.5}$) is plotted in Figure 6d and corresponding fitting parameters are given in Table 3. Weber–Morris plots of Im-IONP, hetero-IOCC, and homo-IOCC samples comprise two steps: 1) external surface adsorption or the diffusion of CV and CR molecules to the surface of adsorbent materials, which continues till the exterior surface reaches the saturation; and then 2) the internal diffusion of dye molecules within the pores, also known as intraparticle diffusion, reaching the final equilibrium step.^[60] The slope of the linear part of each curve could give the rate constants and the intercepts (I) could be obtained from the extrapolation of the first step in the curves to the time axis (Figure 6d). It was found that the extrapolation of initial linear graphs does not pass through the origin, which strongly indicates the influence of boundary layers on the adsorption process.

3.6.3. Adsorption Isotherm Studies

Adsorption isotherms are critical to getting an insight into the adsorption mechanism and the maximum adsorption capacity and understanding the feasibility of the application purpose. Here, Langmuir and Freundlich isotherm models were used to study the adsorption isotherms. The Langmuir model can describe the monolayer adsorption onto a surface with a finite number of identical sites whereas the Freundlich isotherm models were used to describe the sorption onto a heterogeneous surface.

The nonlinear form of the Langmuir isotherm is given as follows:

$$q_e = \frac{q_{\max} K_L C_e}{1 + K_L C_e} \quad (7)$$

where C_e is the CR concentration in equilibrium (mg L⁻¹), q_{\max} represents maximum adsorption capacity (mg g⁻¹), and K_L is the Langmuir constant (L mg⁻¹).

The nonlinear form of the Freundlich isotherm model equation is given as follows:

$$q_e = K_F C_e^{1/n} \quad (8)$$

where K_F and n are the Freundlich constants related to adsorption capacity and adsorption intensity, respectively.

Effect of Initial Concentration: Adsorption isotherms were further investigated and further fitted by the nonlinear Langmuir and Freundlich isotherm model to evaluate the dye adsorption performance of hetero-IOCC, homo-IOCC, and Im-IONP. The fitted parameters are shown in Table S2, Supporting Information. For a better understanding of the adsorption mechanism, an aqueous solution of 5–50 mg L⁻¹ dye concentration was used for the isotherm experiment at room temperature, which is presented in Figure 7a,b. The adsorption capacities of the CV dye for hetero-IOCC sample increase from 12.55 to 64.62 mg g⁻¹ while the adsorption capacities of the CR dye for hetero-IOCC sample increase from 28.3 to 130.92 mg g⁻¹ as the initial dye concentration increases from 5 to 50 mg L⁻¹. This observation could be explained by the fact that a high concentration of dye represents a stronger driving force between adsorbent and liquid phases thereby enhancing the adsorption rate. Compared to the nonlinear Freundlich isotherm model ($R^2 = 0.91$), the Langmuir isotherm model of $R^2 = 0.97$ was more suitable to describe the adsorption mechanism indicating the possibility of homogenous monolayer adsorption.^[61] From the fitting of adsorption data with the Langmuir isotherm model, the theoretical values for the adsorption capacity for CR dye for hetero-IOCC, homo-IOCC, and Im-IONP samples were found to be (140.19 ± 14.10), (17.95 ± 1.43), and (53.19 ± 2.81) mg g⁻¹, respectively. Also, the theoretical values for the adsorption capacities for CV dye for the hetero-IOCC, homo-IOCC, and Im-IONP samples were found to be (71.63 ± 7.15), (12.51 ± 0.62), and (48.17 ± 5.6) mg g⁻¹, respectively. The adsorption performance of the CV and CR dyes for the samples are compared with the existing reports and shown in Table 4.

Effect of Adsorbent Dosage: The dose of adsorbent can strongly influence the adsorption capacity; so, the adsorption experiment was carried out by varying the sample dose from 0.2 to 1 g L⁻¹ on 10 mg L⁻¹ dye solution. With the initial adsorbent dosage of the sample increasing from 0.2 to 1 g L⁻¹, the adsorption capacities of the CV dye decreased from 35.45 to 5.92 mg g⁻¹ and the adsorption capacities of the CR dye decreased from 45.84 to 9.912 mg g⁻¹, indicating their good adsorption capacities at the lower sample dose concentration, as shown in Figure 7c,d. The same trend of decrease in adsorption capacity with the increase in adsorbent concentration holds good for the homo-IOCC and Im-IONP samples also. The decrease in the adsorption capacity (q_e) value with the increase of adsorbent dose might be because of the presence of greater surface area for a fixed amount of adsorbate.^[62] The effectiveness of low adsorbent dose shows that it could be beneficial to treat the pollutants that are present even in small trace amounts in water bodies.

Effect of pH: pH of a medium is critical for determining the role of the adsorption process by altering surface charge and ionization of both adsorbent as well as adsorbate. The dependence of dye adsorption on pH can be evaluated from the perspective of surface chemistry in an aqueous phase. Generally, the surfaces

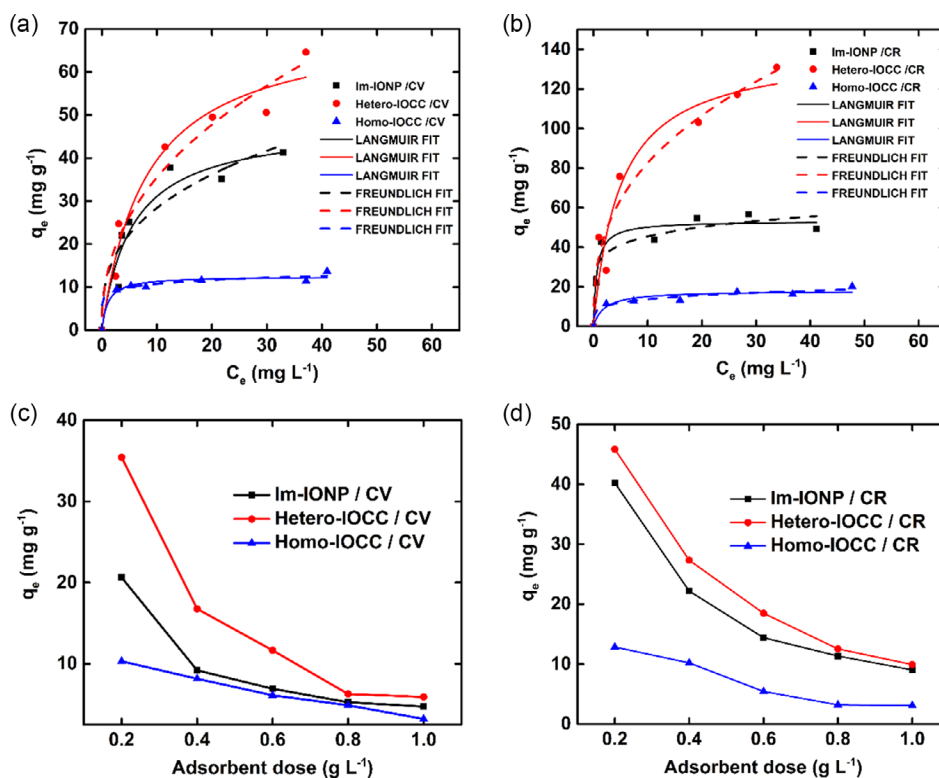


Figure 7. Adsorption isotherm of a) CV and b) CR dye on sample fitted with Freundlich isotherm model and Langmuir isotherm model; [Adsorbent dose: 0.2 g L^{-1} , initial dye concentration: 5 to 50 mg L^{-1} , pH 7] Influence of dose concentration on the adsorption capacity of c) CV and d) CR dye [Adsorbent dose: 0.2 – 1 g L^{-1} , initial dye concentration: 10 mg L^{-1} , pH 7].

Table 4. Comparison of the maximum adsorption capacities (q_{max}) of variously reported sorbents for CV and CR. (BTCA: Benzenetetracarboxylic acid, SPION: superparamagnetic iron oxide nanoparticle. IO: iron oxide, PANI: polyaniline, BNNS: boron nitride nanosheets).

Sorbent	Synthesis method	Dye	pH	Dye concentration [mg L^{-1}]	Adsorbent dose [g L^{-1}]	q_{max} [mg g^{-1}]	Rem-oval %	References
Jute fiber carbon	Carbonization	CV	8	40	0.2	27.99		[66]
Nonmagnetic IO	Entrapment method		9	5	0.1	16.50		[67]
IO based on κ -carrageenan-g poly (methacrylic acid) nanocomposite	Co-ppt		8	50	0.5	28.24		[68]
BTCA- Fe_3O_4	Co-ppt		10	20	0.02		14	[15]
SPION	Co-ppt		9	10	8		20	[69]
Hetero-IOCC	Co-ppt and Calcination		7	50	0.2	71.63	53.40	Present work
Homo-IOCC						12.51	18.60	
Im-IONP	Co-ppt					48.17	41.40	
Pretreated Fe_3O_4	Co-ppt	CR	6.6	30	4	21.28		[70]
Activated carbon	Ultrasound-assisted method		4	200	0.2	14.92		[71]
$\text{Au-Fe}_3\text{O}_4$ -NCs-AC			4	200	0.2	21.05		
Activated carbon (ultrasound)			4	200	0.2	24.65		
BNNS@ Fe_3O_4	High pressure			200	0.33		39	[72]
PANI/ Fe_3O_4	Polymerization and mixing			20	0.1	21.38		[73]
MnFe_2O_4	Co-ppt		6.6	30	4	25.78		[70]
Fe_3O_4 @ SiO_2 Magnetic NPs	Co-ppt		5.5	30	2	24		[74]
Hetero-IOCC	Co-ppt and calcination		7	50	0.2	140.19	74.40	Present work
Homo-IOCC						17.95	10.10	
Im-IONP	Co-ppt					53.19	60.70	

of iron oxides are covered with $-\text{OH}^-$ groups either from the adsorbed water molecules or from the structures of metal oxide that vary in form at different pH levels. These groups have two pairs of electrons together with a dissociable H-atom that enables them to react to both acids and bases. Accordingly, it was reported that the major dominant functional groups of iron oxide surface would be Fe^{2+} or FeOH^+ at lower pH (acidic) and $\text{Fe}(\text{OH})_2$ and $\text{Fe}(\text{OH})_3^{-1}$, which are its hydrolysis products, at the higher pH (basic medium). So, it was expected that the iron oxide adsorbent adsorbed anionic dyes better at lower pH and cationic dye better at higher pH.^[63] Thus, the adsorption capacity of CR dyes on hetero-IOCC was reduced from 72.41 to 10.69 mg g^{-1} when the pH increased from 3 to 12. In contrast, the adsorption capacities of CV dyes on hetero-IOCC were increased from 9.4 mg g^{-1} at pH 3 to 45.85 mg g^{-1} at high pH 12 (Figure 8). To evaluate the relation between the surface charge of the adsorbents and the pH of the solution in the adsorption process, the surface potential of the three samples: hetero-IOCC, homo-IOCC, and Im-IONP were measured at neutral pH (pH 7) and were found to be -18.6 , -13.3 , and -10.1 mV, respectively. As all three samples had nearly the same negative potential, the surface potentials of the best-performing hetero-IOCC sample were measured at five different pH values namely, pH 3, 5, 7, 9, and 12 and plotted as a function of pH to determine the point of zero charge (PZC). The PZC of hetero-IOCC was found to be 6.2 (Figure 8c). This suggested that the surface charge of the adsorbent at $\text{pH} < \text{PZC}$ was positive and at $\text{pH} > \text{PZC}$ was negative. So, the anionic CR dyes were expected to be adsorbed better at low pH and the cationic CV dye was envisaged to be adsorbed better at higher pH, which was in agreement with our experimental results.

Thermodynamic Study: The thermodynamic study for the most efficient hetero-IOCC sample was carried out to study the effect of temperature variation on the adsorption capacity of the adsorbents. The thermodynamics parameters were also evaluated, using the Van't Hoff plots (shown in Figure 9b). With the aqueous solution temperature increased from 305 to 325 K with initial dye solutions of 10 mg L^{-1} and an adsorbent dose of 0.2 g L^{-1} at pH 7, the hetero-IOCC sample exhibited an increasing trend of adsorption capacities for CR dyes. This rise in adsorption capacity could be due to the enhanced mobility of CR ions onto the adsorbent nanoparticles. However, the adsorbents showed a slightly decreasing trend of adsorption

capacity with the increase of temperature for CV dyes, as shown in Figure 9a.

The thermodynamic parameters viz., the change in Gibbs free energy (ΔG), entropy (ΔS), and enthalpy (ΔH) can be evaluated by using Van't Hoff's equations:

$$\ln(K_d) = \left(\frac{\Delta S}{R}\right) - \left(\frac{\Delta H}{R}\right) \quad (9)$$

$$\Delta G = -RT \ln(K_d) \quad (10)$$

$$K_d = \frac{q_e}{C_e} \quad (11)$$

where K_d is the distribution coefficient for the adsorption process.

The slope and intercept of the $\ln(K_d)$ versus $1/T$ graph can be used to calculate enthalpy (ΔH) and entropy (ΔS) respectively of the adsorption process and the corresponding values of thermodynamic parameters are listed in Table 5. The negative value of ΔG in all cases indicates the spontaneity and feasibility of the adsorbent sample in a wide range of temperatures. For the adsorption process in hetero-IOCC, the positive value of ΔH for CV dye indicates the endothermic nature of the adsorption process whereas the negative value of ΔH for CR dye indicates the exothermic process. Additionally, the negative ΔS value for CV dye adsorption depicts the decrease in randomness or disorders at the interface while the positive ΔS value for CR dye suggests the increase in the randomness or disorders of the system. Generally, the positive value of ΔH reflects the chemisorption and electrostatic-based interaction for the CV dyes while the negative value of ΔH for CR dye indicates the physical interactive force could be dominating force for CR adsorption.^[64]

3.6.4. Effect of Different Coexisting Ions

Most industrial wastewater generally contains plenty amount of salts of wide ionic strength, that can greatly alter the adsorption capacities of various dyes. To evaluate the influence of ions on dye adsorption, two commonly used salts namely, NaCl and MgCl_2 , were mixed at various concentrations 10, 50, 100, and 200 g L^{-1} with the dye solution, prepared at 10 mg L^{-1} . The variation of dye adsorption with the increase of the ionic strength is presented in Figure 9c,d. The decrease in CV and

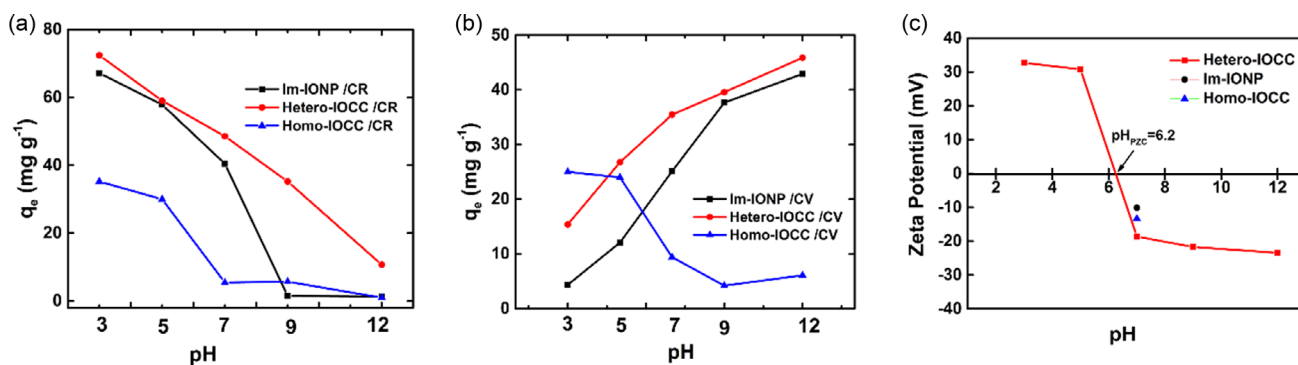


Figure 8. Influence of pH on a) CR and b) CV adsorption on Im-IONP, hetero-IOCC, and homo-IOCC; c) Variation of zeta potential with pH to determine point of zero charge.

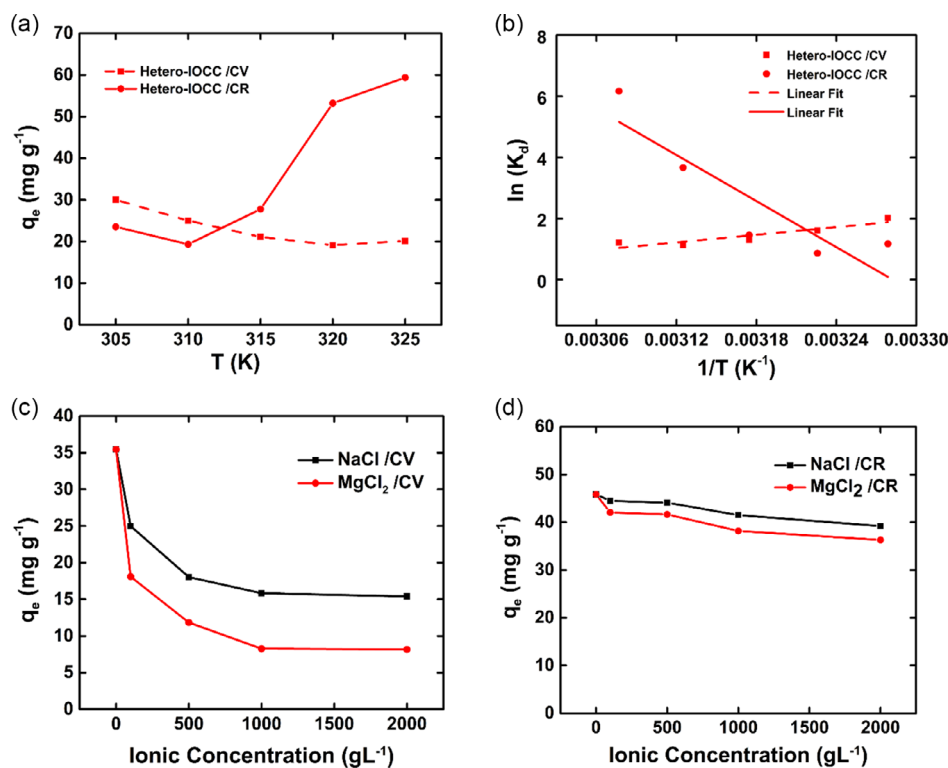


Figure 9. a) Variation of adsorption capacities of CR and CV at different temperature, b) Vant Hoff's plot for thermodynamic study of hetero-IOCC, and influence of NaCl and MgCl₂ on the adsorption capacity of c) CV and d) CR dyes on hetero-IOCC samples.

Table 5. Thermodynamic parameters for the adsorption of CV and CR dyes onto hetero-IOCC, homo-IOCC, and Im-IONP.

Temperature [K]	CV			CR		
	ΔG [KJ mol ⁻¹]	ΔH [KJ mol ⁻¹]	ΔS [KJ mol ⁻¹]	ΔG [KJ mol ⁻¹]	ΔH [KJ mol ⁻¹]	ΔS [KJ mol ⁻¹]
305	-5.11	34.65	-97.94	-2.97	-209.10	686.321
310	-4.12			-2.23		
315	-3.40			-3.82		
320	-3.01			-9.76		
325	-3.28			-16.68		

CR adsorption capacity with the rise in ionic concentration of NaCl and MgCl₂ salts could be because the salt molecules present in the solution occupy some of the active sites present in the adsorbent. So there could be competition between cationic dye particles and cations present in the solution for the active sites on the adsorbent.

3.6.5. Adsorption Mechanism

To analyze the adsorption mechanism of CR and CV dyes, FTIR spectra of hetero-IOCC, homo-IOCC, and Im-IONP before and after dye adsorptions were recorded, as shown in **Figure 10**. The peaks located at ≈ 1065 cm⁻¹ correspond to the vibration of the sulfonic group of CR. This vibrational band is observed clearly in the FTIR peaks of hetero-IOCC, homo-IOCC, and Im-IONP, which are examined after the adsorption of CR dye. Also,

≈ 1455 and ≈ 1585 cm⁻¹ vibrational bands which belong to the -NH₂ and -N=N aromatic group, respectively, affect the vibration bands of the Im-IONP after adsorption.^[65] Moreover, the peak intensities of the CR dye which are observed in the FTIR spectra of the sample after adsorption are reduced. These findings point to the adsorption of CR dye onto the surface of the Im-IONP. Electrostatic interaction between the negative charge sulfonic group and H⁺ forming SO₃H at around 1169 cm⁻¹ which is commonly observed in the CR dye adsorption was not observed. Similarly, the vibrational bands at ≈ 1160 , ≈ 1296 , ≈ 1351 , ≈ 1580 , ≈ 2923 , and ≈ 3303 cm⁻¹ correspond to stretching vibration of C-H in the aromatic ring, C-N vibration, C=C stretching vibrations in aromatic nuclei, N=H stretching vibration of amino group, and -OH bond of water adsorbed on CV, respectively. These vibrational bands were found to affect the FTIR spectra of hetero-IOCC, homo-IOCC, and Im-IONP

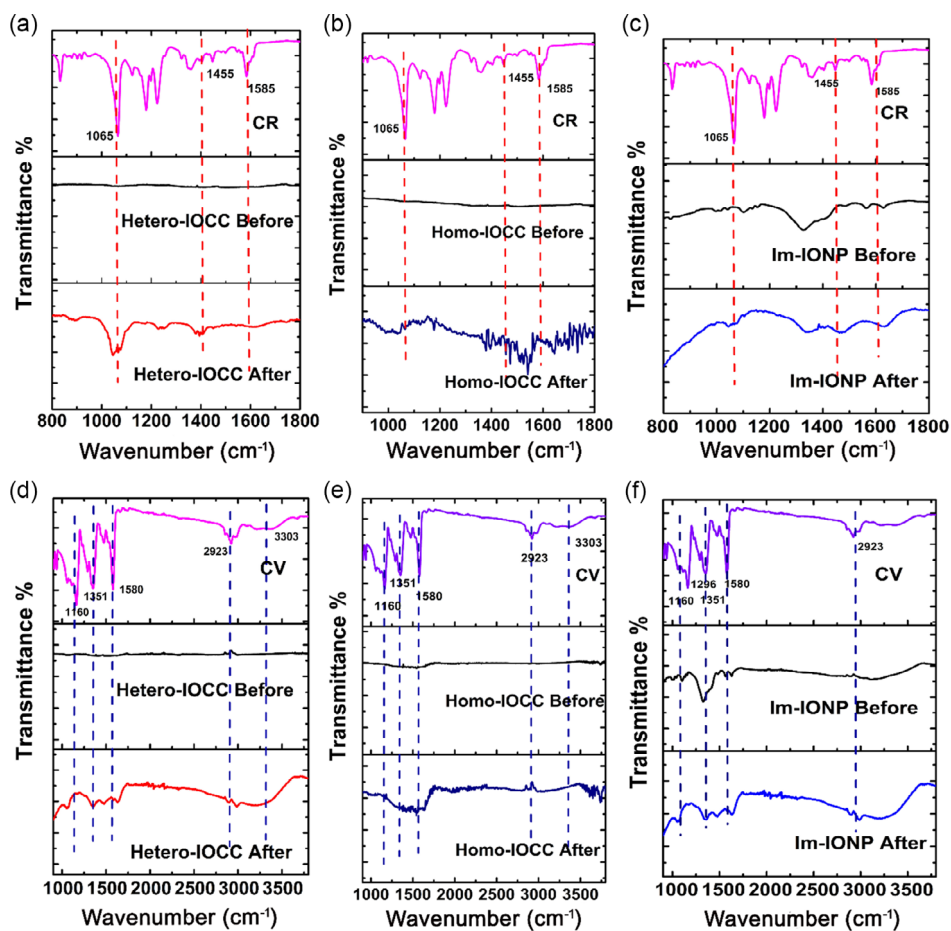


Figure 10. FTIR of hetero-IOCC, homo-IOCC, and Im-IONP samples before and after adsorption for a–c) CR [in the range of 800–1800 cm^{-1}] and d–f) CV dyes [in the range of 900–3800 cm^{-1}].

taken after the adsorption, which confirms the adsorption of CV. The possible mechanism underlying the adsorption process of CV and CR onto hetero-IOCC, homo-IOCC, and Im-IONP, as shown in Scheme 2, mainly involves van der Waals and hydrogen bonding, which could be related to shifting of the aromatic vibrational bands. Moreover, ion exchange, π - π interactions and hydrophobic interactions may also be involved in the process.

3.6.6. Regeneration of Adsorbent

To ensure efficient sequestration of pollutants from water bodies, the materials should have the ability to be separated easily and recycled without much reduction in their removal capacities. So, the regeneration and reusability of adsorbents are of immense importance from the perspective of practical application. Batch adsorption and desorption cycles were carried out to explore the reusability capacity of these samples. As shown in **Figure 11**, the reusability capacity of hetero-IOCC samples is greater in removal capacity (>50%) even after three cycles both for the CR and CV dyes, whereas both other samples viz., homo-IOCC and Im-IONP reduce significantly. In addition to the better performance on dye removal, hetero-IOCC adsorbent has the

extra advantage of the ease of separation using a magnet for further use.

4. Conclusion

In conclusion, iron oxide/carbon composite with heterophase grain boundaries (hetero-IOCC) is successfully synthesized by calcining the imidazole-capped SPM α - Fe_2O_3 (Im-IONP), which was obtained from the coprecipitation of iron nitrate and 2-methyl imidazole solutions. The spectroscopic studies elucidate that the oxidation to α - Fe_2O_3 favored the agglomeration, whereas the γ - Fe_2O_3 was observed to have preserved the size experiencing the SPM properties. While implemented as an active material for dye adsorption, hetero-IOCC exhibited superior dye adsorption with a capacity of 71.63 and 140.19 mg g^{-1} for both the cationic CV and anionic CR dyes respectively, compared to the Im-IONP (48.17 and 53.19 mg g^{-1}) and homo-IOCC (12.51 and 17.95 mg g^{-1}) at an initial dye concentration of 50 mg L^{-1} , pH 7, and adsorbent dose of 0.2 g L^{-1} . Adsorption isotherms and kinetic studies suggest that the Langmuir isotherm model was found to be an appropriate model following the Elovich kinetic model. The enhanced dye adsorption in hetero-IOCC is attributed to the 1) heterophase grain boundaries

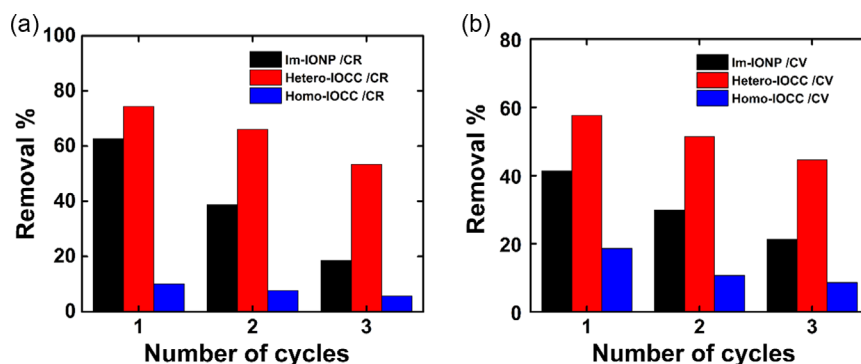


Figure 11. Reusability of Im-IONP, hetero-IOCC, and homo-IOCC adsorbents under three consecutive adsorption and desorption cycles; [initial dye concentration of 10 mg L^{-1} , pH 7, and adsorbent dose of 0.2 g L^{-1}].

among the $\alpha\text{-Fe}_2\text{O}_3$ and $\gamma\text{-Fe}_2\text{O}_3$ which provide many active sites; 2) the presence of carbon coating which protects NPs from the agglomerations; and 3) the charged defects that got induced on the grain boundaries facilitate both the surface and intraparticle diffusion of both the cationic and anionic dyes. We anticipate that the strategy can be adopted to design and synthesize unique metal oxide/carbon composites with heterophase grain boundaries for a wide range of applications such as catalysis, gas sensors, hydrogen evolution reactions, energy storage, and sustainable wastewater treatment.

Supporting Information

Supporting Information is available from the Wiley Online Library or from the author.

Acknowledgements

K.P.S. would like to extend gratitude to UGC for providing the fellowship and financial support. L.H.S. would like to thank DST-SERB for the financial assistance under the project having file no. CRG/2021/001611. S.G. acknowledges Marie Skłodowska-Curie postdoctoral fellowship (101067998 — ENHANCER). The authors thank the Department of Chemistry, NIT Manipur for the XRD, zeta potential, and FTIR measurements. The author also thanks Daniel Cliff Gonmei, Department of Physics, NIT Manipur for his valuable support in the synthesis process. The author would like to thank Devidas TR, Post-Doctoral Fellow, Bar Ilan University for his valuable insight in the review process. The author would like to thank Mr. Subhadip Pal for support in characterizations. The author also would like to acknowledge SAIF, IIT Bombay for providing the HRTEM facility for my research work. The advanced characterization facilities—VSM and TGA/DTA provided by the Centre for Instrumental Facility (CIF) at IIT Guwahati and XPS provided by the Institute Instrumentation Centre at IIT Roorkee are also acknowledged.

Conflict of Interest

The authors declare no conflict of interest.

Author Contributions

K.P.S.: Conceptualization, data curation, formal analysis, writing original draft, review and editing; B.W.: Investigation, review and Editing; R.K.G.:

Investigation; N.J.S.: Formal analysis; A.C. de O.: Investigation; V.K.G.: Investigation; S.G.: Investigation, supervision, review, and editing; L.H.S.: Supervision, methodology, investigation, project administration, writing, and review; resources, visualization, funding acquisition.

Data Availability Statement

The data that support the findings of this study are available from the corresponding author upon reasonable request.

Keywords

dye adsorptions, grain boundaries, iron oxides, nanostructures, superparamagnet, wastewater treatment

Received: March 13, 2023

Revised: August 30, 2023

Published online:

- [1] H. Anwer, A. Mahmood, J. Lee, K. H. Kim, J. W. Park, A. C. K. Yip, *Nano Res.* **2019**, *12*, 955.
- [2] S. Dutta, B. Gupta, S. K. Srivastava, A. K. Gupta, *Mater. Adv.* **2021**, *2*, 4497.
- [3] R. K. Verma, *Biointerface Res. Appl. Chem.* **2021**, *12*, 567.
- [4] S. Xu, Y. Jin, R. Li, M. Shan, Y. Zhang, *J. Colloid Interface Sci.* **2022**, *607*, 890.
- [5] N. Y. Donkadokula, A. K. Kola, I. Naz, D. Saroj, *Rev. Environ. Sci. Bio/ Technol.* **2020**, *19*, 543.
- [6] H. Nawaz, M. Umar, I. Nawaz, A. Ullah, M. Tauseef Khawar, M. Nikiel, H. Razzaq, M. Siddiq, X. Liu, *Adv. Eng. Mater.* **2022**, *24*, 2100719.
- [7] V. Binas, A. Philippidis, A. Zachopoulos, G. Kiriakidis, *Adv. Eng. Mater.* **2017**, *19*, 1600661.
- [8] S. Afshin, Y. Rashtbari, M. Vosoughi, R. Rehman, B. Ramavandi, A. Behzad, L. Mitu, *Rev. Chim.* **2020**, *71*, 218.
- [9] J. K. Sahoo, S. K. Paikra, M. Mishra, H. Sahoo, *J. Mol. Liq.* **2019**, *282*, 428.
- [10] N. Hassan, A. Shahat, A. El-Didamony, M. G. El-Desouky, A. A. El-Bindary, *J. Mol. Struct.* **2020**, *1217*, 128361.
- [11] A. S. Eltaweil, A. M. El-Tawil, E. M. Abd El-Monaem, G. M. El-Subruiti, *ACS Omega* **2021**, *6*, 6348.
- [12] A. V. Anupama, W. Keune, B. Sahoo, *J. Magn. Magn. Mater.* **2017**, *439*, 156.

- [13] Y. Liu, Q. Liu, L. Wang, X. Yang, W. Yang, J. Zheng, H. Hou, *ACS Appl. Mater. Interfaces* **2020**, *12*, 4777.
- [14] Q. Yang, H. Song, Y. Li, Z. Pan, *J. Mol. Liq.* **2017**, *234*, 18.
- [15] S. Chatterjee, N. Guha, S. Krishnan, A. K. Singh, P. Mathur, D. K. Rai, *Sci. Rep.* **2020**, *10*, 1.
- [16] M. Li, G. Wu, Z. Liu, X. Xi, Y. Xia, J. Ning, D. Yang, A. Dong, *J. Hazard. Mater.* **2020**, *397*, 122766.
- [17] Q. Liu, Y. Li, H. Chen, J. Lu, G. Yu, M. Möslang, Y. Zhou, *J. Hazard. Mater.* **2020**, *382*, 121040.
- [18] T.-S. Kim, H. J. Song, M. A. Dar, H.-J. Lee, D.-W. Kim, *Appl. Surf. Sci.* **2018**, *439*, 364.
- [19] N. J. Singh, B. Wareppam, A. Kumar, K. P. Singh, V. K. Garg, A. C. Oliveira, L. H. Singh, *J. Mater. Res.* **2022**, *65*, 1149.
- [20] B. Saiphaneendra, T. Saxena, S. A. Singh, G. Madras, C. Srivastava, *J. Environ. Chem. Eng.* **2017**, *5*, 26.
- [21] C. Li, W. Li, H.-Y. Zhao, X.-Y. Feng, X. Li, Z.-Z. Yu, *Nano Res.* **2023**, *16*, 6343.
- [22] M. Verma, I. Tyagi, V. Kumar, S. Goel, D. Vaya, H. Kim, *J. Environ. Chem. Eng.* **2021**, *9*, 106045.
- [23] A. A. Basaleh, M. H. Al-Malack, T. A. Saleh, *J. Environ. Chem. Eng.* **2021**, *9*, 105126.
- [24] Q. Zhang, I. Castellanos-rubio, R. Munshi, I. Orue, B. Pelaz, K. I. Gries, W. J. Parak, P. Pino, A. Pralle, *Chem. Mater.* **2015**, *27*, 7380.
- [25] K. Simeonidis, C. Martinez-Boubeta, D. Serantes, S. Ruta, O. Chubykalo-Fesenko, R. Chantrell, J. Oró-Solé, L. Balcells, A. S. Kamzin, R. A. Nazipov, A. Makridis, M. Angelakeris, *ACS Appl. Nano Mater.* **2020**, *3*, 4465.
- [26] Y. Liu, X. Zou, L. Li, Z. Shen, Y. Cao, Y. Wang, L. Cui, J. Cheng, Y. Wang, X. Li, *J. Colloid Interface Sci.* **2021**, *599*, 795.
- [27] J. Zhuang, F. He, X. Liu, P. Si, F. Gu, J. Xu, Y. Wang, G. Xu, *Nano Res.* **2022**, *15*, 1230.
- [28] A. M. Omar, O. I. Metwalli, M. R. Saber, G. Khabiri, M. E. M. Ali, A. Hassen, M. M. H. Khalil, A. A. Maarouf, A. S. G. Khalil, *RSC Adv.* **2019**, *9*, 28345.
- [29] M. Balakrishnan, R. John, *Iran. J. Catal.* **2020**, *10*, 1.
- [30] M. T. Thanh, T. V. Thien, P. D. Du, N. P. Hung, D. Q. Khieu, *J. Porous Mater.* **2018**, *25*, 857.
- [31] M. Chen, E. Zhao, Q. Yan, Z. Hu, X. Xiao, D. Chen, *Sci. Rep.* **2016**, *6*, 29381.
- [32] J. Du, H. Liu, *J. Magn. Magn. Mater.* **2006**, *302*, 263.
- [33] U. S. Khan, Amanullah, A. Manan, N. Khan, A. Mahmood, A. Rahim, *Mater. Sci.-Pol.* **2015**, *33*, 278.
- [34] H. Ismail, Z. Zainuddin, H. Mohamad, M. A. A. Hamid, *J. Phys. Sci.* **2022**, *33*, 61.
- [35] R. Khan, M. Ur, R. Zainab, *J. Mater. Sci.: Mater. Electron.* **2016**, *27*, 12490.
- [36] C. J. Serpell, J. Cookson, P. D. Beer, *ChemistryOpen* **2020**, *9*, 683.
- [37] S. Ayyappan, G. Gnanaprakash, G. Panneerselvam, M. P. Antony, J. Philip, *J. Phys. Chem. C* **2008**, *112*, 18376.
- [38] C. Feng, Y. Guo, S. Qiao, Y. Xie, L. Zhang, L. Zhang, W. Wang, J. Wang, *Appl. Surf. Sci.* **2020**, *533*, 147481.
- [39] N. Hellgren, R. T. Haasch, S. Schmidt, L. Hultman, I. Petrov, *Carbon* **2016**, *108*, 242.
- [40] S. Jain, J. Shah, N. S. Negi, *Int. J. Energy Res.* **2019**, *43*, 4743.
- [41] S. Ghosh, S. R. Polaki, G. Sahoo, E.-M. Jin, M. Kamruddin, J. S. Cho, S. M. Jeong, *J. Ind. Eng. Chem.* **2019**, *72*, 107.
- [42] C. Hu, X. Hu, R. Li, Y. Xing, *J. Hazard. Mater.* **2020**, *385*, 121599.
- [43] D. Talbot, J. Q. Campos, B. L. Checa-fernandez, J. A. Marins, C. Lomenech, C. Hurel, G. D. Godeau, M. Raboisson-michel, G. Verger-dubois, L. Obeid, P. Kuzhir, A. Bee, *ACS Omega* **2021**, *6*, 19086.
- [44] B. Wareppam, E. Kuzmann, V. K. Garg, L. H. Singh, *J. Mater. Res.* **2023**, *38*, 937.
- [45] J. Lee, S. Kwak, *ACS Omega* **2018**, *3*, 2634.
- [46] C. Qiu, F. Cai, Y. Wang, Y. Liu, Q. Wang, C. Zhao, *J. Colloid Interface Sci.* **2020**, *565*, 351.
- [47] S. Wang, J. Cui, S. Zhang, X. Xie, W. Xia, *Mater. Res. Express* **2020**, *7*, 025304.
- [48] Y. Shen, W. Li, J. Wu, S. Li, H. Luo, S. Dai, W. Wu, *Dalton Trans.* **2014**, *43*, 10023.
- [49] A. Lassoued, B. Dkhil, A. Gadri, S. Ammar, *Results Phys.* **2017**, *7*, 3007.
- [50] M. D. Patekari, K. K. Pawar, G. B. Salunkhe, P. M. Kodam, M. N. Padvi, P. P. Waifalkar, K. K. Sharma, P. S. Patil, *Mater. Sci. Eng., B* **2021**, *272*, 115339.
- [51] L. Herojit Singh, R. Govindaraj, G. Amarendra, C. S. Sundar, *J. Phys. Chem. C* **2013**, *117*, 25042.
- [52] T. Truong, T. M. Hoang, C. K. Nguyen, Q. T. N. Huynh, N. T. S. Phan, *RSC Adv.* **2015**, *5*, 24769.
- [53] H. Ullah, K. S. Qureshi, U. Khan, M. Zaffar, Y. J. Yang, N. E. Rabat, M. I. Khan, S. Saqib, A. Mukhtar, S. Ullah, M. Mubashir, A. Bokhari, W. S. Chai, K. W. Chew, P. L. Show, *Chemosphere* **2021**, *285*, 131492.
- [54] X. Xu, Y. Liu, J. Wang, D. Isheim, V. P. Dravid, C. Phatak, S. M. Haile, *Nat. Mater.* **2020**, *19*, 887.
- [55] K. Sato, *J. Phys. Chem. C* **2017**, *121*, 20407.
- [56] A. Sikiru, O. A. Ajayi, L. Taofeek, *Sci. Afr.* **2021**, *13*, e00850.
- [57] P. Sun, C. Hui, R. A. Khan, J. Du, Q. Zhang, Y. H. Zhao, *Sci. Rep.* **2015**, *5*, 1.
- [58] M. Makrygianni, A. Christofili, V. Deimede, *Colloids Surf., A* **2021**, *610*, 125634.
- [59] S. Pashaei-Fakhri, S. J. Peighambari, R. Foroutan, N. Arsalani, B. Ramavandi, *Chemosphere* **2021**, *270*, 129419.
- [60] M. A. E. Barakat, R. Kumar, M. K. Seliem, A. Q. Selim, M. Mobarak, I. Anastopoulos, D. Giannakoudakis, M. Barczak, A. Bonilla-Petriciolet, E. A. Mohamed, *Nanomaterials* **2020**, *10*, 1.
- [61] R. Foroutan, R. Mohammadi, N. Sohrabi, S. Sahebi, S. Farjadfar, Z. Esvandi, B. Ramavandi, *Environ. Technol. Innovation* **2020**, *17*, 100530.
- [62] B. Saha, S. Das, J. Saikia, G. Das, *J. Phys. Chem. C* **2011**, *115*, 8024.
- [63] S. R. Chowdhury, E. K. Yanful, A. R. Pratt, *J. Hazard. Mater.* **2012**, *235–236*, 246.
- [64] S.-H. Kim, P.-P. Choi, *Dalt. Trans.* **2017**, *46*, 15470.
- [65] M. S. Gopika, S. Jayasudha, P. B. Nair, *Mater. Sci.* **2022**, *45*, 71.
- [66] K. Porkodi, K. Vasanth Kumar, *J. Hazard. Mater.* **2007**, *143*, 311.
- [67] S. Hamidzadeh, M. Torabbeigi, S. J. Shahtaheri, *J. Environ. Health Sci. Eng.* **2015**, *13*, 8.
- [68] M. Gholami, M. T. Vardini, G. R. Mahdavinia, *Carbohydr. Polym.* **2016**, *136*, 772.
- [69] A. V. Samrot, H. Hashma, J. S. A. E. Faradjeva, P. Raji, P. Prakash, S. K. S, *Curr. Res. Green Sustainable Chem.* **2021**, *4*, 100066.
- [70] L. Yang, Y. Zhang, X. Liu, X. Jiang, Z. Zhang, T. Zhang, L. Zhang, *Chem. Eng. J.* **2014**, *246*, 88.
- [71] E. A. Dil, M. Ghaedi, A. Asfaram, A. A. Bazrafshan, *Ultrason. Sonochem.* **2018**, *46*, 99.
- [72] J. Yang, J. Shang, J. Chen, F. Xue, Z. Ke, X. Zhang, E. Ding, *J. Polym. Res.* **2021**, *28*, 1.
- [73] X. P. Teng, M. Y. K. Bryan, P. V. Chai, J. Y. Law, *Mater. Today Proc.* **2021**, *46*, 1875.
- [74] C.-R. Lin, O. S. Ivanova, D. A. Petrov, A. E. Sokolov, Y.-Z. Chen, M. A. Gerasimova, S. M. Zharkov, Y.-T. Tseng, N. P. Shestakov, I. S. Edelman, *Nanomaterials* **2021**, *11*, 2371.